Sunish Vadakkeveetil,[1] *Arash Nouri,*[2] *and Saied Taheri*[3]

Comparison of Analytical Model for Contact Mechanics Parameters with Numerical Analysis and Experimental Results

REFERENCE: Vadakkeveetil, S., Nouri, A., and Taheri, S., **"Comparison of Analytical Model for Contact Mechanics Parameters with Numerical Analysis and Experimental Results,"** *Tire Science and Technology,* TSTCA, Vol. 48, No. 3, July–September 2020, pp. 168–187.

ABSTRACT: Being able to estimate tire/rubber friction is very important to tire engineers, materials developers, and pavement engineers. This is because of the need for estimating forces generated at the contact, optimizing tire and vehicle performance, and estimating tire wear. Efficient models for contact area and interfacial separation are key for accurate prediction of friction coefficient. Based on the contact mechanics and surface roughness, various models were developed that can predict real area of contact and penetration depth/interfacial separation. In the present work, we intend to compare the analytical contact mechanics models using experimental results and numerical analysis. Nano-indentation experiments are performed on the rubber compound to obtain penetration depth data. A finite element model of a rubber block in contact with a rough surface was developed and validated using the nano-indentation experimental data. Results for different operating conditions obtained from the developed finite element model are compared with analytical model results, and further model improvements are discussed.

KEY WORDS: friction, Hertzian contact mechanics, penetration depth, nano-indentation, finite element, sliding contact

Introduction

Contact friction is an important phenomenon in most tribological applications. It determines the tractive effort that is required to ensure proper functionality at the contact. One of the main factors that affects the friction at the contact interface is contact area and deformation [*1–3*]. Developments in the surface measurement devices with the capability of measuring up to resolution of atomic scale have found that the surface that appears smooth to the unaided eye has some level of roughness as the length scale is decreased or the magnification is increased. This further has an influence on the contact area and other contact mechanics parameters such as penetration depth and contact pressure.

[1] Corresponding author. Department of Mechanical Engineering, Virginia Polytechnic Institute and State University, 100 B Randolph Hall, 460 Old Turner Street, Blacksburg, Virginia 24060, USA. Email: sunish90@vt.edu

[2] Department of Mechanical Engineering, Virginia Polytechnic Institute and State University, 100 B Randolph Hall, 460 Old Turner Street, Blacksburg, Virginia 24060, USA. Email: anouri@vt.edu

[3] Department of Mechanical Engineering, Virginia Polytechnic Institute and State University, 100 C Randolph Hall, 460 Old Turner Street, Blacksburg, Virginia 24060, USA

Contact mechanics is a study of deformation of the bodies occurring at the contact interface due to the relative motion with respect to each other. Experimental observations [*4*] in the past have shown that due to surface roughness at higher magnification, the real area of contact is only a portion of the complete contact area. Because of its influence in obtaining the contact interfacial shear stresses, responsible for friction, it is very important to consider surface roughness when developing an accurate contact mechanics model. Various contact theories [*5–7*] were developed in the past based on continuum theories and assuming linear elastic isotropic medium and stochastic models to represent the surface roughness. Previous work was focused on obtaining the influence of normal load or pressure on friction and contact mechanics parameters. It was found that though Persson's contact mechanics model [*8*] shows a linear relation of the contact area, the friction coefficient was found to have no influence on normal load variations mainly due to consideration of the complete contact [*9,10*]. The Kluppel model [*11,12*], on the other hand, considered a Hertzian based approach using the Greenwood Williamson (GW) model [*6*] for the contact mechanics and obtained the variation of friction coefficient with load mainly due to consideration of partial contact by obtaining the penetration depth. Finite element [*13–15*] approaches were also developed for estimation of the contact mechanics parameters and friction using periodic boundary condition and different length scales. Experimental analysis for measuring the contact mechanics parameters is a difficult task, and static measurements using photogrammetry and nano-indentation experiments are used for comparison with simplified analytical models.

The present work mainly focuses on comparing the analytical models with numerical and experimental analysis. The paper starts with a discussion on the analytical models that are used for comparison in the "Theory" section; the "Numerical Approach" section describes different numerical approaches that are considered and the material model that will be used for the simulation, followed by the nano-indentation experimental testing, discussed in the "Experimental Testing" section. The "Results and Discussion" section discusses the results and compares the different models considered, followed by a conclusion of the study in the "Conclusion" section.

Theory

Hertz Contact Theory

Hertz contact theory predicts the contact mechanics of two perfectly smooth non-confirming elastic half spaces [*5*]. The deformations are obtained by assuming point contact on an elastic half space with no tangential motion and considering Boussinesq-Cerrutti potential function as shown in Fig. 1. A boundary condition for no penetration of the surface for point in contact is

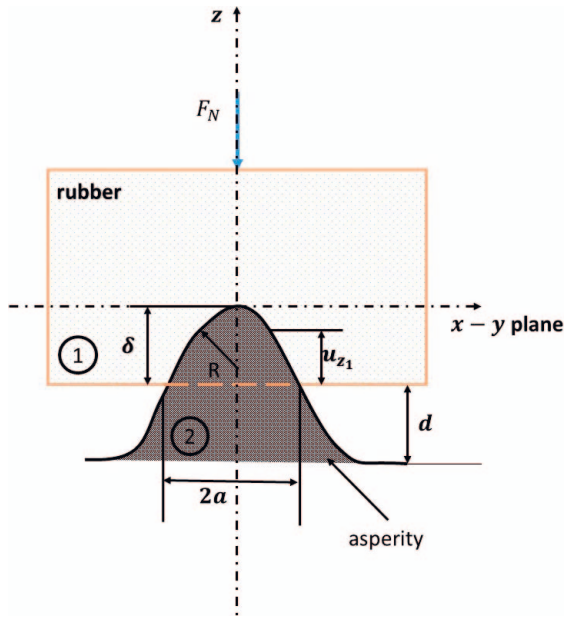

FIG. 1 — *Hertz contact of plane surface with spherical asperity.*

considered.

$$u_{z1} + u_{z2} + h = \delta \tag{1}$$

where u_{z1} and u_{z2} are the deformations of a point on the surface of each body, respectively, δ is the approach distance at the center of the contact, and h is the relative profile of the surface. In the case of a plane surface in contact with a spherical body, the contact mechanics parameters for a Hertz pressure distribution at the contact is given by contact radius as

$$a = \pi p_0 R / 2E^* \tag{2}$$

Approach distance of a distant point in the center of the contact is given by

$$\delta = \frac{\pi p_0 a}{2E^*} \tag{3}$$

Total load on the solids is given by

$$P = \frac{2}{3} p_0 \pi a^2 \tag{4}$$

where p_0 is the maximum amplitude of the pressure, R is the radius of the spherical elastic half space, and E^* is the relative modulus of both bodies given by

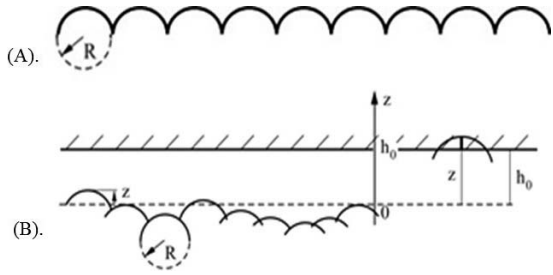

FIG. 2 — *(A) Identical asperities; (B) spherical asperities with height distribution.*

$$\frac{1}{E^*} = \frac{1-\nu_1^2}{E_1} + \frac{1-\nu_2^2}{E_2} \tag{5}$$

If one material is considered rigid then the relative modulus of the contact is represented by a plane stress equation given by

$$\frac{1}{E^*} = \frac{1-\nu^2}{E} \tag{6}$$

Greenwood Williamson Theory

Hertz contact theory can be employed for contact of a plane surface with a rigid surface, where the asperities are considered to be spherical with identical radius of curvature and height, as shown in Fig. 2A. The total load and contact area in this case will be the sum of all local loads and contact areas on each asperity obtained using Eqs. (2)–(4). However, the real surfaces are rough with random height distribution. In order to consider this situation, Greenwood Williamson [*6*] considers the surface with spherical asperities and identical radius but with a height distribution. It is assumed that the contact only occurs in the summits of the asperities and the interactions of the neighboring asperities are neglected.

Under these conditions, the number of summits above a certain distance d form the mean profile is obtained using

$$n = N \int_d^\infty \phi_s(z)dz \tag{7}$$

where N is the total number of summit asperities, $\phi_s(z)$ is the summit height distribution of the surface, and d is the surface distance from the mean. Similar to the identical asperity case, the total contact area and the total normal load is the sum of the individual asperities given by

$$F_N = \frac{4}{3} N R^{1/2} E^* \int_d^\infty (z-d)^{3/2} \phi_s(z)dz \tag{8}$$

$$A = N\pi R \int_d^\infty (z-d)\phi_s(z)dz \tag{9}$$

$$\sigma_0' = \frac{16}{9}E'(\omega_{\min})R^{\frac{1}{2}}N_s\widetilde{\sigma}_s \int_d^\infty \left(z - \frac{d}{\widetilde{\sigma}_s}\right)^{3/2} \phi_s(z)dz \tag{10}$$

where F_N is the normal load, A is the contact area, macro asperity radius of curvature is $R = \xi_{||}^2/4\pi^2\xi_\perp$, $N_s = \xi_{||}^{-2}$ is the density of the summit, d is the separation of the surfaces or the separation distance, $\widetilde{\sigma_s}$ is the standard deviation of the summit heights, and $F_n(t)$ is the Greenwood Williamson (GW) function. In general form, the integrand in Eqs. (7)–(9) can be represented using the GW function given by

$$F_n(d) = \int_d^\infty (z-d)^n \phi_s(z)dz \tag{11}$$

Extension of Greenwood Williamson Theory

In the case of GW theory, the contact is assumed to occur only at the summits of the contact, and coupling of length scales or different magnifications are not considered. For contact parameters governed by the large length scale asperities like the true contact stress and the mean penetration depth, this approximation will work. However, at lower length scales, the rubber tries to fill the surface asperities, and hence the internal contact area in the cavities apart from the external contact area must be considered (shown in Fig. 3).

In order to estimate the true contact area and the bounding frequencies, energy condition of elastic contact as a function of the length scale given by Eq. (12) is considered [*12*]. It states that the sum of the deformation work due to the normal force and adhesion energy should be greater than the elastic stored energy due the local deformation of rubber

$$\sigma(\lambda)\lambda^2 h(\lambda) + \Delta\ \gamma\ \lambda\ h(\lambda) \gtrsim E'(\lambda)h^3(\lambda) \tag{12}$$

where λ is the length scale, $h(\lambda)$ is the roughness amplitude of the surface at the particular length scale, $\Delta\gamma$ is the change in the interfacial energy given by $\Delta\gamma = \gamma_1 + \gamma_2 - \gamma_{12}$, and $E'(\lambda)$ is the real part of the viscoelastic modulus.

Numerical Approach

The numerical analysis is performed using the commercial finite element software, ABAQUS. In this section, the finite element model developed for simulation of nano-indentation, representing the different properties, is discussed. Additionally, a rubber block sliding on a rough surface and the respective material models are also discussed.

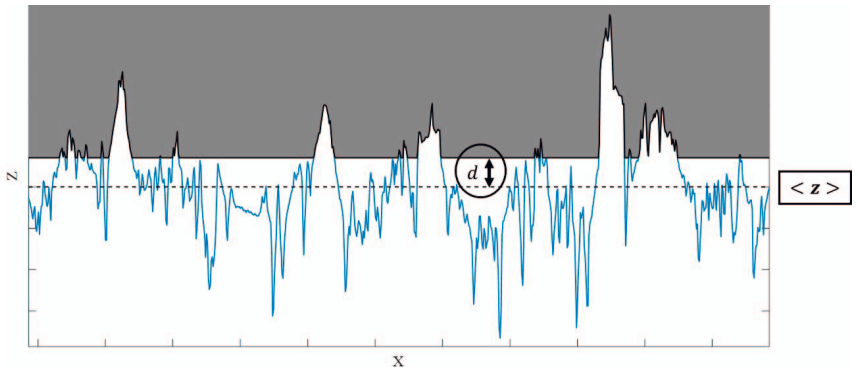

FIG. 3 — *Deformation at the contact interface representing the mean surface profile* $< z >$ *and mean separation distance d.*

Material Model

Hyperelastic model. In order to perform numerical simulations, the material properties for the rubber sample have to be determined. A hyperelastic material model obtained based on the uniaxial tensile test data of the rubber sample was considered. Based on the material evaluation tool available in ABAQUS and considering the uniaxial test data, the Mooney Rivlin model was found to agree well with the test data.

The strain energy equation of the Mooney Rivlin model is given by

$$W = C_{10}(\overline{I_1} - 3) + C_{01}(\overline{I_2} - 3) + \frac{1}{D_1}(J^{\text{el}} - 1)^2 \tag{13}$$

where C_{01}, C_{10}, and D_1 are material parameters obtained using experimental test data (material evaluation tool in ABAQUS), I_1 and I_2 are first and second deviatoric invariants, and J^{el} is the elastic volume ratio. In this case, rubber being an incompressible material, the elastic volume ratio term will vanish.

Prony series for viscoelastic properties. For this study, the Prony (Dirichlet) series was used for analytical representation of viscoelastic materials. This method is beneficial for describing the broadband behavior of the viscoelastic materials regarding their exponential components, as well their computational efficiency [*16,17*]. In fact, this method deals with broadband behavior by mapping each series of the test data into the Laplace domain and converting it to the frequency domain. In this paper, a comprehensive study was done to fit a Prony series on the data by having the minimum number of components. To do that, the Prony series was fitted on the data with a different number of Prony coefficients starting from 2 to 15. The mean square error (MSE) was used as an indicator for selecting the best fit with minimum possible number of Prony coefficients.

As mentioned earlier, the main goal of this section is to calculate the Prony series coefficients (g_i and τ_i) by fitting the real and loss or imaginary modulus of the material (G_R and G_I) obtained using experiments to the Prony equation given by

$$G_R^{\text{est}} = G_0(1 - \sum_i^N \bar{g}_i^p) + G_0 \sum_i^N \frac{\bar{g}_i^p \tau_i^2 \omega^2}{1 + (\tau_i \omega)^2}$$

$$G_I^{\text{est}} = G_0 \sum_i^N \frac{\bar{g}_i^p \tau_i \omega}{1 + (\tau_i \omega)^2} \tag{14}$$

where G_0 is the instantaneous modulus at high frequencies and G_∞ is the long-term modulus at low frequencies. The following formula

$$\chi^2 = \sum_i^M \frac{1}{G_\infty^2} \left((G_R^{\text{exp}} - G_R^{\text{est}})_i^2 + (G_I^{\text{exp}} - G_I^{\text{est}})_i^2 \right) \tag{15}$$

was used to calculate the loss function considering the experimental and estimated storage and loss modulus, which is minimized to obtain an optimum fit. However, based on the literature, there are some constraints applied to the selection of each of the values. The summary of applied constraints is given by

$$\tau_i > 0; \quad \bar{g}_i^p > 0$$

$$\tau_{i+1} > \tau_i$$

$$\sum \bar{g}_i^p < 1 \tag{16}$$

In addition, data used for the fit were limited between 10^{-5} and 10^{13} Hz (Fig. 4). The *LMFIT* [*18*] package in Python was used for doing the least square fit on the value for different length of components. Figure 5 shows the summary of MSE for each fit with different numbers of Prony coefficients. It should be noted that for each coefficient number the best initial conditions were sought.

As the results show, the best fit was achieved by using 11 coefficients. Figure 6 illustrates the final results of the estimated modulus using the model.

Nano-Indentation Model

Nano-indentation is a type of depth-sensing indentation measurement technique used for measurement of penetration of a rigid indenter tip into a softer material at constant loading or displacement rate [*19*]. It is mainly used for measuring mechanical properties of indented material such as hardness/stiffness or bulk material properties from creep/relaxation data [*20*].

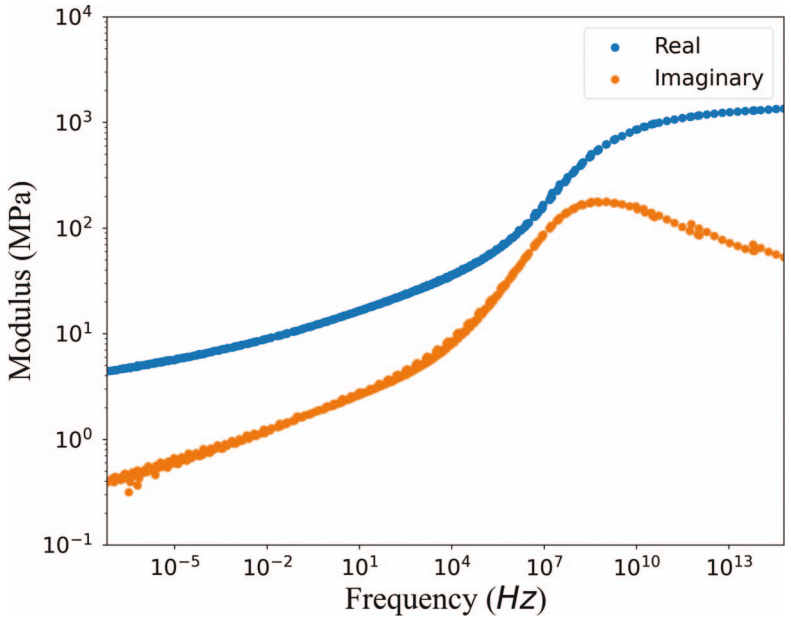

FIG. 4 — *Raw material modulus data used for obtaining the Prony series.*

The simulation model for the nano-indentation is shown in Fig. 7. An axisymmetric model is considered for both the indenter and the rubber sample. The indenter is modeled as a discrete rigid sphere with the diameter equivalent to the radius of curvature of the indenter used for experimental testing, 5 μm.

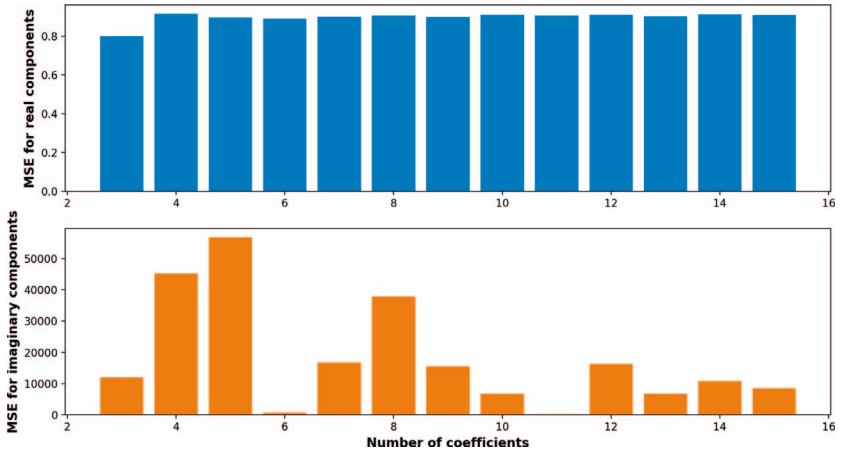

FIG. 5 — *Mean square error (MSE) for both real and imaginary components.*

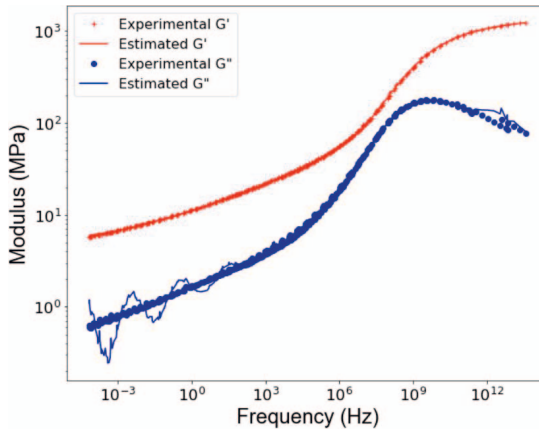

FIG. 6 — *Final results after fitting using the Prony equation.*

The rubber sample is modeled as a deformable body with the rubber material properties as described in Table 1. The rubber sample is discretized with a minimum element size of 1 μm near the contact region and a maximum element size of 5 μm near the end. A bilinear axis symmetric quadrilateral element (CAX4RH) with reduced integration and hourglass constraint is assigned to the rubber sample.

A surface-to-surface contact is assigned between the indenter and the rubber sample with a penalty contact algorithm and considering the friction coefficient to be 0. The rubber block is fixed at the bottom, and a displacement type of loading is applied to the indenter center as shown in Fig. 7. The reaction

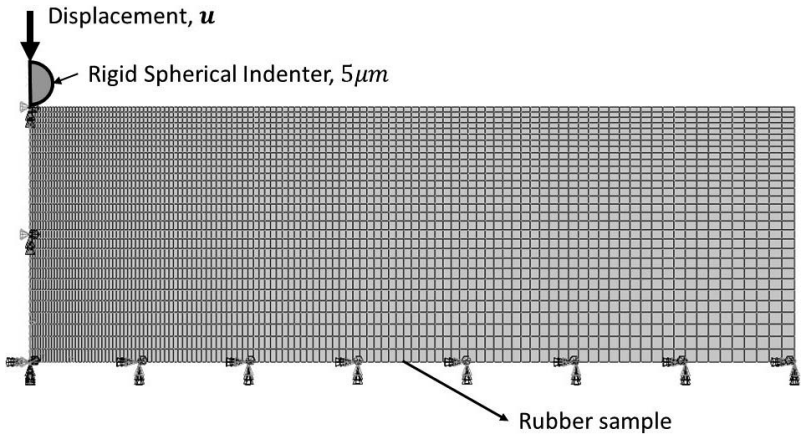

FIG. 7 — *Nano-indentation simulation model.*

TABLE 1 — *Material property information for a compound a rubber sample.*

Mooney Rivlin parameters for hyperelastic properties	
C_{10}, 1.627×10^{-2}	
C_{01}, 7.004×10^{-2}	
Prony series constants for viscoelastic properties	
$G0$, 1300 Pa	
g_1, 0.35	τ_1, 1×10^{-15}
g_2, 0.289	τ_2, 1×10^{-10}
g_3, 0.28	τ_3, 1×10^{-9}
g_4, 0.0393	τ_4, 1×10^{-7}
g_5, 0.0138	τ_5, 1×10^{-5}
g_6, 0.00706	τ_6, 1×10^{-2}
g_7, 0.00473	τ_7, 1×10^{-1}
g_8, 0.00284	τ_8, 1×10^{2}
g_9, 0.00188	τ_9, 1×10^{3}
g_{10}, 0.00366	τ_9, 1×10^{13}
g_{11}, $5.417e^{-6}$	τ_{11}, 1×10^{15}

force thus measured is used for comparison with analytical and experimental results.

Rubber Block Sliding on Rough Substrate

A simple rectangular cross section of a tread block is considered to be sliding on a rigid plane surface as shown in Fig. 8. ABAQUS Explicit analysis is performed for the sliding simulation. The surface considered is modeled as

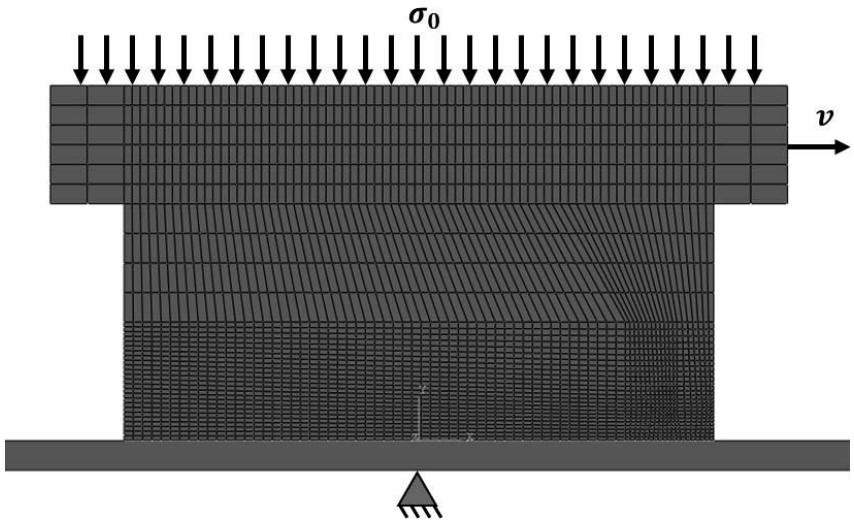

FIG. 8 — *Rubber block sliding on a rigid surface.*

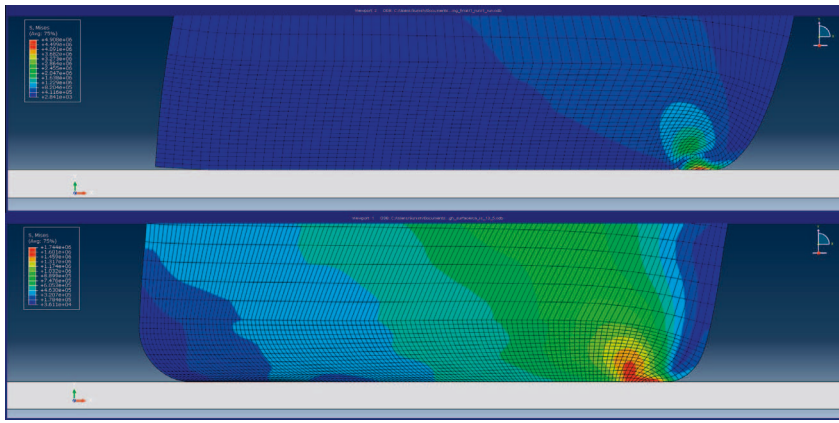

FIG. 9 — *Comparison of rubber block with sharp edges (top) vs rounded edged (bottom).*

discrete and rigid, and the rubber sample is considered to be a deformable body with the material properties shown in Table 1. Hourglass constraint (CPE4R) is considered, and the rectangular sample is discretized using a bilinear quadrilateral element with reduced integration. In order to consider the model similar to the analytical problem, it is assumed to have large displacements in the lateral direction with respect to sliding direction so as to simplify the problem to plain strain. A finer element discretization is considered toward the leading edge of the rubber block.

A surface-to-surface penalty contact algorithm with a contact friction of zero is considered between the rubber sample and the rigid surface. All nodes in the top surface of the block, where the loading is applied, are coupled to have the same displacements in the loading direction. A two-step analysis is considered for the simulation. The rigid surface is fixed in all directions, and a pressure loading condition is applied to the top surface of the rubber block as part of step one. In the second step, keeping the load fixed, a sliding velocity is applied to the top surface of the block.

Results of the simulation performed using the present configuration (flat bottom surface) are as shown in Fig. 9 (top). It shows a buckling phenomenon [*13*] occurring at the leading edge of the rubber block, which is mainly due to the sharp edges at the leading edge of the contact generating an uneven distribution of pressure at the contact interface. Hence, in order to eliminate this buckling phenomena, the edges are rounded as shown in Fig. 9 (bottom).

Experimental Testing

In order to test the accuracy of our numerical and analytical models, the penetration depth results at different normal loads or pressures are compared

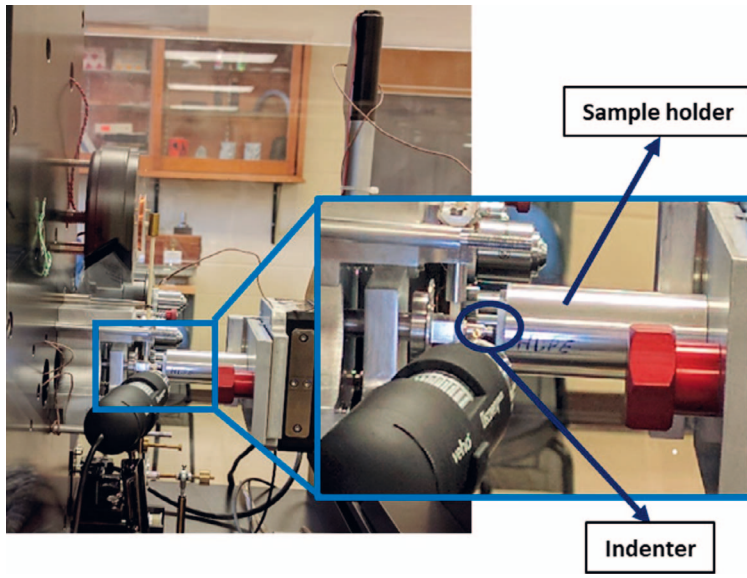

FIG. 10 — *Nano-indentation equipment.*

with experimental results obtained using the nano-indentation experiment, where penetration depth at different loads is measured. The results thus obtained are used for comparison with the simplified numerical and analytical models.

NanoTest system, a flexible nano-mechanical property measurement system from Micro Materials available in the BEAM department of Virginia Tech, as shown in Fig. 10, is used for nano-indentation measurements of Compound A rubber sample (provided by Bridgestone). A rigid spherical indenter of size 5 μm is used for the experiment and the rubber sample of size 15 mm × 15 mm is mounted on the sample holder using an adhesive. A gradually increased loading at a constant rate up to a desired value is applied followed by creep loading for a certain time to obtain the penetration measurement.

Since the experiments are performed in micro scale, different factors are to be considered to ensure validity of the results obtained. Creep test is performed to obtain an optimum creep time, and a repeatability at a constant load is performed to ensure that sample surface roughness does not affect the data measured.

A creep test is performed on the rubber sample by applying a step load of 2 mN and then holding it constant for a certain period. The penetration depth vs time readings are as shown in Fig. 11. The deformation increases rapidly initially and then reaches a constant value after a certain period, which in this

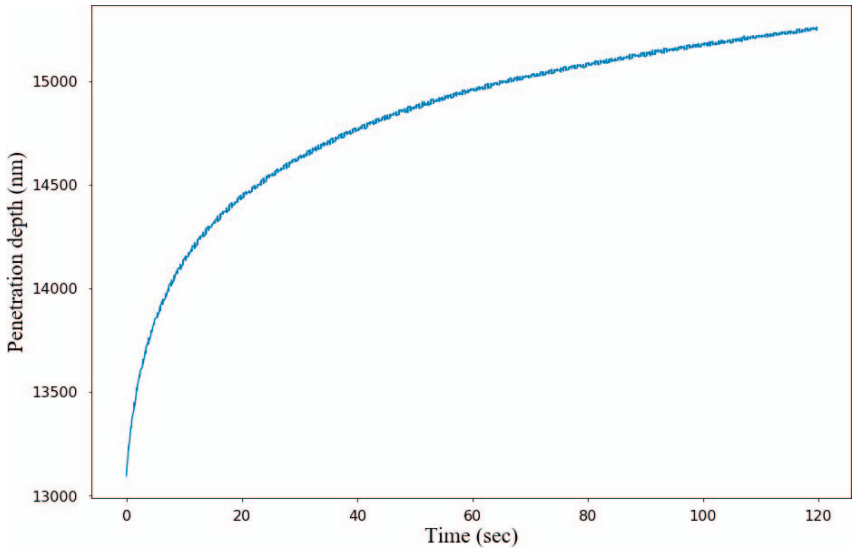

FIG. 11 — *Creep test of Compound A sample with a maximum load of 2 mN.*

case is considered 60 seconds because the deformation tends to reach a constant value (approximately 3% at 120 seconds).

In order to make sure there is no influence of the surface roughness on the measurement data [*21*], repeatability of the experiment is also performed under a maximum load of 2 mN at a constant loading rate while maintaining the load for 60 seconds (based on the creep test results) at eight different locations on the rubber sample. The peak penetration depth was observed to be equivalent between the tests (with a maximum error of 4%) as shown in Fig. 12.

After obtaining an optimum creep time and ensuring the repeatability of the experiment, the indentation experiment is performed at nine different loads, and penetration depths are obtained. The results are shown in Fig. 13. The peak penetration and the contact area

$$A = 2\pi Rh \tag{17}$$

under different loading conditions are shown in Figs. 13–14. Next, the experimental test data will be compared with simple numerical and analytical models.

Results and Discussion

Simulations are performed on a Compound A sample (provided by Bridgestone) that is sliding on 120-grit sandpaper. The viscoelastic material

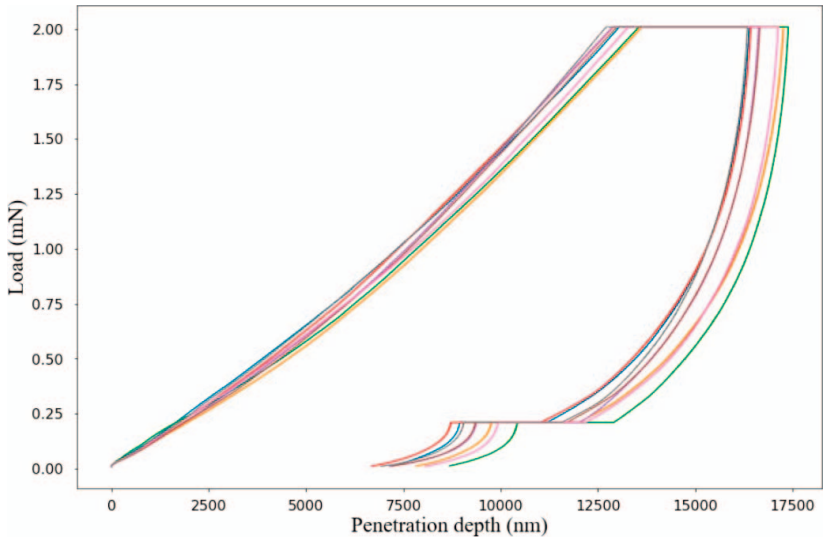

FIG. 12 — *Repeatability of loading step up to 2 mN at eight different spots in the rubber sample.*

property of the sample is obtained using dynamic mechanical analysis (DMA) testing as shown in Fig. 15A, and the surface profile of the 120-grit surface is obtained using the Nanovea Jr25 profilometer with a resolution of 7 μm as shown in Fig. 15B.

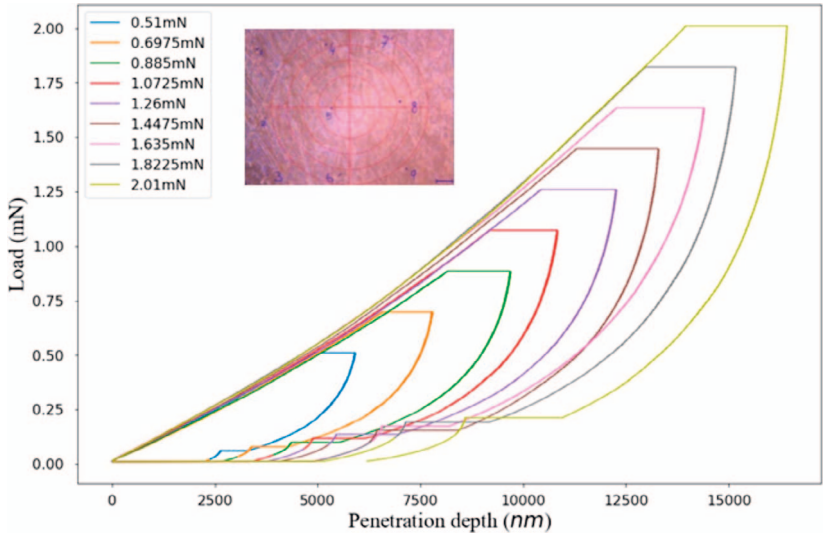

FIG. 13 — *Indentation depth vs load for nine different loads from 0.5 to 2 mN.*

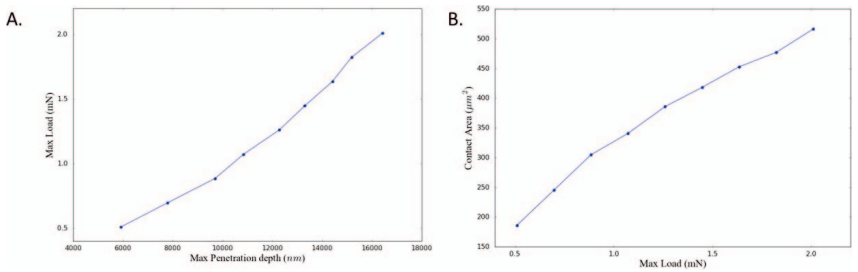

FIG. 14 — *(A) Maximum load vs penetration depth; (B) contact area at maximum load.*

In order to test the numerical and the analytical models, a simplified model is considered for both cases. For obtaining the analytical results, the Hertz contact theory between a flat surface and a spherical indenter is used, and the radius of curvature is considered similar to the one used for experimental testing. The numerical model of the nano-indentation, as was shown in Fig. 7, is solved under different displacement conditions, and the results are shown in Fig. 16.

The reaction force under each displacement loading obtained from experiments is compared with the simple Hertz model and is shown in Fig. 17. There is a maximum error of 8% when comparing the experimental data with the numerical model.

Based on the similar criterion of the indentation simulation, the numerical analysis of a rubber block sliding on a rough substrate is performed using ABAQUS explicit. The measured surface profile of the 120-grit sandpaper is imported to ABAQUS as a discrete rigid surface (shown in Fig. 18A). Simulation of a rubber block sliding on the rough substrate is performed with the similar boundary conditions as described in the "Rubber Block Sliding on Rough Substrate" section for different loads and velocities. In order to obtain the mean separation distance, the deformation of the rubber block contact interface is measured and the difference calculated with respect to the mean surface profile.

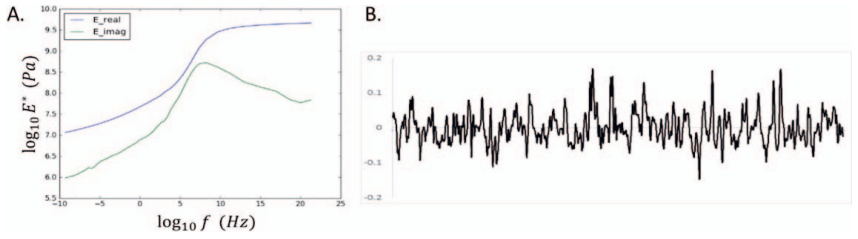

FIG. 15 — *(A) DMA master curve data for Compound A; (B) surface profile for 120-grit surface.*

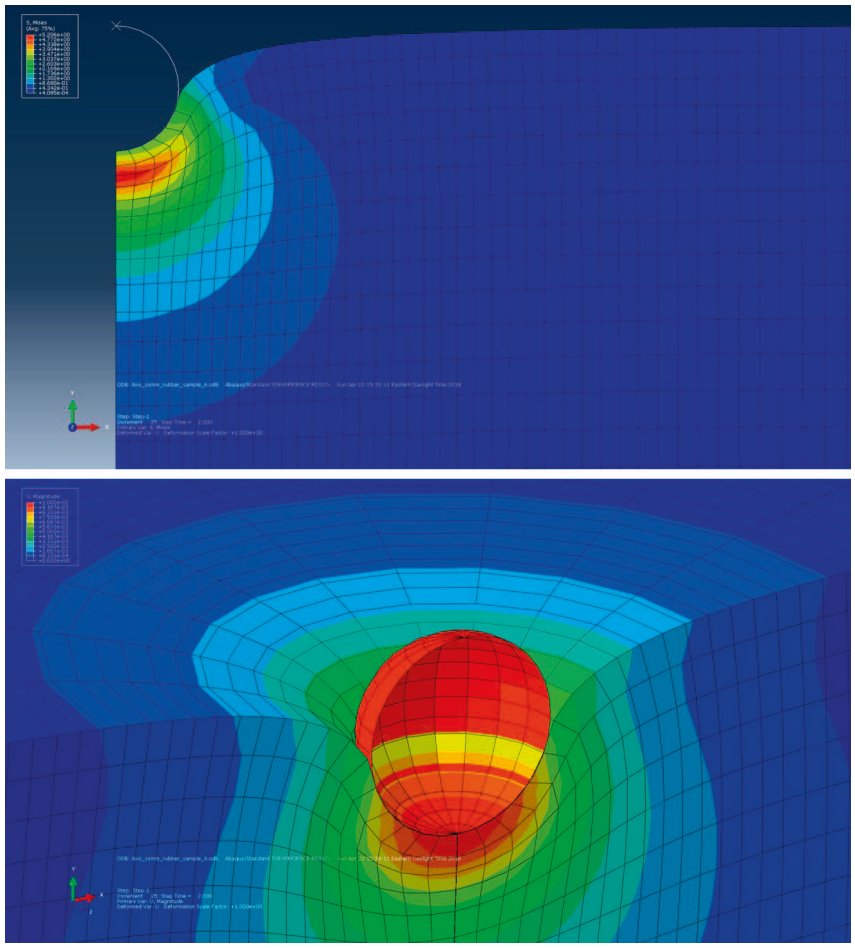

FIG. 16 — *Axisymmetric indentation simulation of a spherical sphere on a flat rubber sample.*

The deformation of the rubber block at the contact interface measured for different conditions is plotted against the road profile. As shown in Fig. 19, with increase in the load, there is an increase in the penetration depth of the rubber block. The mean separation distance for different operation conditions is obtained by considering the mean deformations of the contact interface and mean height of the surface profile and is shown in Fig. 20A. Under different operating conditions, the deformation of the contact interface for the numerical case is calculated after the rubber block has traversed the same distance. Based on the results, the mean separation distance is observed to be constant as a function of the sliding velocity with a slight variation at lower velocities and a decrease in the separation distance as the normal load or pressure increases.

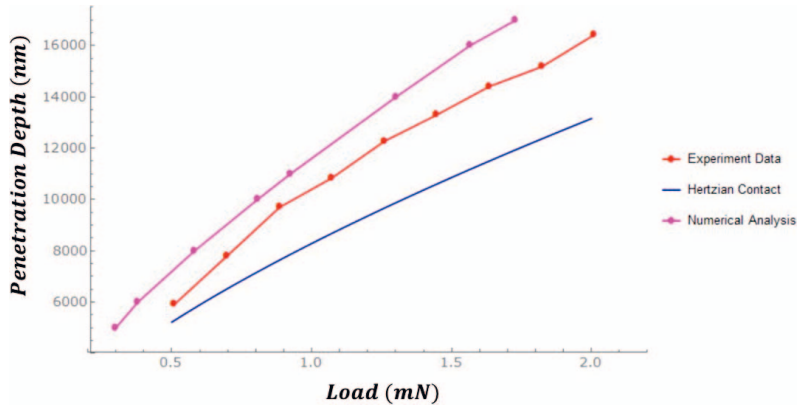

FIG. 17 — *Comparison of analytical (Hertz theory), numerical analysis using finite elements and experimental testing.*

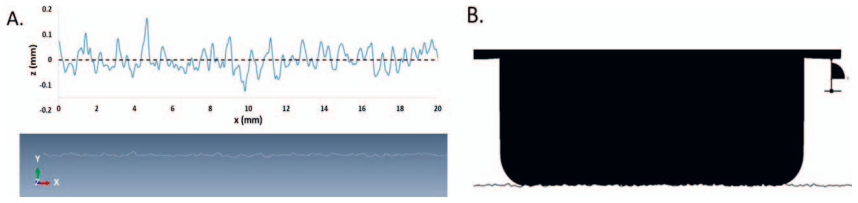

FIG. 18 — *(A) Surface profile in ABAQUS; (B) model of the rubber block sliding on a rough substrate.*

The simulation results of the analytical model are obtained using the extended GW theory developed by Klüppel, as described in the "Greenwood Williamson Theory" section. The GW function is obtained from the height distribution of the 120-grit surface profile, as shown in Fig. 21.

The mean separation distance is then calculated by solving Eq. (10) for different operating conditions of sliding velocity and normal load. The results thus obtained are compared with numerical simulation as shown in Fig. 20B.

In the case of analytical simulation, there is small variation of the mean separation distance with respect to the sliding velocity that tends to a constant value at higher velocities. When comparing the influence of mean separation distance to the normal load or pressure, the distance reduces as the pressure decreases due to increased deformation of the contact interface. Hence, there is a qualitative agreement between the numerical analysis and the analytical simulation, with the results being in the same order of magnitude. The variations between the results can be attributed to the more dynamic and viscous nature of the numerical analysis, whereas in the developed analytical model linear elasticity assumption was used. In addition, for the analytical model, the

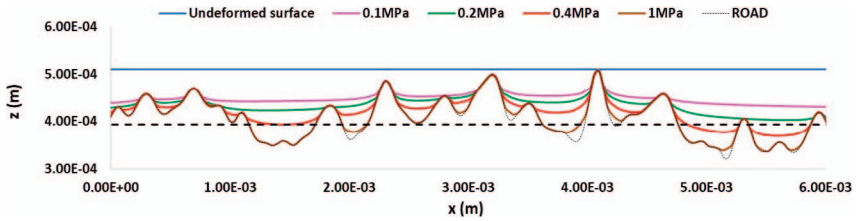

FIG. 19 — *Deformation of the contact interface under different loading conditions.*

neighboring asperity interactions are neglected, which is of importance at higher loads on the overall deformation of the rubber block [*22,23*]. This will be considered in future work.

Conclusions

Accurate estimation of the contact mechanics parameters is key for estimation of contact friction. Validation of the contact mechanics parameters such as contact area and penetration depth under dynamic conditions is a complex task. In this work, numerical simulation using a commercial FE software, ABAQUS, of rubber sliding on a rough substrate was developed and compared with the analytical contact model developed by Klüppel. Additionally, a simplified model of spherical indentation on a rubber sample is developed using ABAQUS under similar conditions, and the results are compared with experimental results obtained using the NanoTest system and also with Hertz theory. It was found that the results agree very well with experimental results with a maximum error of 10%.

Simulation of Compound A rubber block sliding on 120-grit rough surface is performed under different operating conditions and is compared with the results obtained using the contact model from Klüppel. The results agree qualitatively and are in the same order of magnitude. In addition, based on the

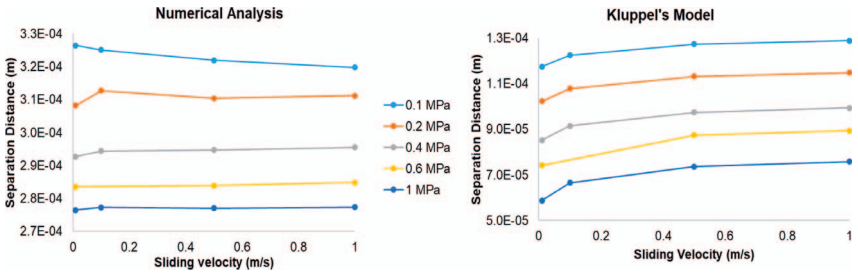

FIG. 20 — *Comparison of separation distance using (left) numerical analysis and (right) analytical model.*

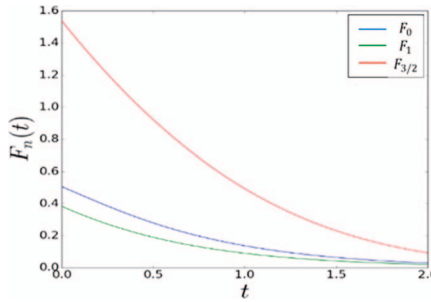

FIG. 21 — *Greenwood Williamson's function.*

simulation results, the penetration depth or separation distance do not vary with sliding velocity. However, these parameters are found to be mostly affected by the normal load or pressure acting at the contact interface. In addition, the variation between the analytical and numerical simulation is attributed to the dynamic nature of the material considered in the numerical simulation as compared with the linear elasticity assumption in the case of the analytical model.

Acknowledgments

The authors would like to thank Bridgestone Americas Operations for providing the rubber sample and material properties for experimental testing, CenTiRe and NSF for their support and funding, and Mac McCord from the Virginia Tech BEAM Department for help with performing nano-indentation experiments.

References

[*1*] Schallamach, A., "The Load Dependence of Rubber Friction," *Proceedings of the Physical Society Section B*, Vol. 65, 1952, pp. 657–661.

[*2*] Grosch, K. A., "The Relation between the Friction and Viscoelastic Properties of Rubber," *Rubber Chemistry and Technology*, Vol. 37, 1964, pp. 386–403.

[*3*] Schallamach, A., "A Theory of Dynamic Rubber Friction," *Rubber Chemistry and Technology*, Vol. 39, 1966, pp. 320–327.

[*4*] Persson, B. N. J., Albohr, O., Tartaglino, U., Volokitin, A. I., and Tosatti, E., "On the Nature of Surface Roughness with Application to Contact Mechanics, Sealing, Rubber Friction and Adhesion," *Journal of Physics: Condensed Matter*, Vol. 17, 2005, pp. R1–R62.

[*5*] Johnson, K. L., "Contact Mechanics," *Journal of the American Chemical Society*, Vol. 37, 1985, pp. 1–17.

[*6*] Greenwood, J. A. and Williamson, J. B. P., "Contact of Nominally Flat Surfaces," *Proceedings of the Royal Society A: Mathematical, Physical, and Engineering Sciences*, Vol. 295, 1966, pp. 300–319.

[7] Bush, A. W., Gibson, R. D., and Thomas, T. R., "The Elastic Contact of a Rough Surface," *Wear*, Vol. 35, 1975, pp. 87–111.

[8] Persson, B. N. J., "Theory of Rubber Friction and Contact Mechanics," *Journal of Chemistry and Physics*, Vol. 115, 2001, pp. 3840–3861.

[9] Vadakkeveetil, S., Emami, A., and Taheri, S., "Pressure Dependent Rubber Friction Model," in *190th International Elastomer Conference Technical Meeting*, Pittsburgh, PA, Oct. 2016. Paper #12.

[10] Fortunato, G., Ciaravola, V., Furno, A., Scaraggi, M., and Lorenz, B., "On the Dependency of Rubber Friction on the Normal Force or Load: Theory and Experiment," *Tire Science and Technology*, Vol. 45, 2017, pp. 25–54.

[11] Gert, H., "Hysteresis Friction of Sliding Rubber on Rough and Fractal Surfaces," *Pochvoznanie i Agrokhimiya*, Vol. 25, 1990, pp. 62–68.

[12] Klüppel, M. and Heinrich, G., "Rubber Friction on Self-Affine Road Tracks," *Rubber Chemistry and Technology*, Vol. 73, 2000, pp. 578–606.

[13] Hofstetter, K., Grohs, C., Eberhardsteiner, J., and Mang, H. A., "Sliding Behaviour of Simplified Tire Tread Patterns Investigated by Means of FEM," *Computers and Structure*, Vol. 84, 2006, pp. 1151–1163.

[14] Wagner, P., Wriggers, P., Klapproth, C., Prange, C., and Wies, B. "Multiscale FEM Approach for Hysteresis Friction of Rubber on Rough Surfaces," *Computer Methods in Applied Mechanics and Engineering*, Vol. 296, 2015, pp. 150–168.

[15] Wagner, P., Wriggers, P., Veltmaat, L., Clasen, H., Prange, C., and Wies, B. "Numerical Multiscale Modelling and Experimental Validation of Low Speed Rubber Friction on Rough Road Surfaces Including Hysteretic and Adhesive Effects," *Tribology International*, Vol. 111, 2017, pp. 243–253.

[16] Park, S. W. and Kim, Y. R., "Fitting Prony-Series Viscoelastic Models with Power-Law Presmoothing," *Journal of Materials in Civil Engineering*, Vol. 13, 2001, pp. 26–32.

[17] Biot, M. A., "Theory of Stress-Strain Relations in Anisotropic Viscoelasticity and Relaxation Phenomena," *Journal of Applied Physics*, Vol. 25, 1954, pp. 1385–1391.

[18] Newville, M., Stensitzki, T., Allen, D. B., Rawlik, M., Ingargiola, A., and Nelson, A., "Lmfit: Non-Linear Least-Square Minimization and Curve-Fitting for Python," *Astrophysics Source Code Library*, 2016. Available at: ascl.net/1606.014.

[19] VanLandingham, M. R., Villarrubia, J. S., Guthrie, W. F., and Meyers, G. F., "Nanoindentation of Polymers: An Overview," *Macromolecular Symposia*, Vol. 167, 2001, pp. 15–43.

[20] Vandamme, M. and Ulm, F. J., "Viscoelastic Solutions for Conical Indentation," *International Journal of Solids and Structures*, Vol. 43, 2006, pp. 3142–3165.

[21] Zhang, T.-Y. and Xu, W.-H., "Surface Effects on Nanoindentation," *Journal of Materials Research*, Vol. 17, 2002, pp. 1715–1720.

[22] Ciavarella, M., Delfine, V., and Demelio, G., "A 'Re-vitalized' Greenwood and Williamson Model of Elastic Contact between Fractal Surfaces," *Journal of the Mechanics and Physics of Solids*, Vol. 54, 2006, pp. 2569–2591.

[23] Afferrante, L., Carbone, G., and Demelio, G., "Interacting and Coalescing Hertzian Asperities: A New Multiasperity Contact Model," *Wear*, Vol. 278–279, 2011, pp. 28–33.